UC Irvine

UC Irvine Previously Published Works

Title

A CMOS MedRadio Transceiver With Supply-Modulated Power Saving Technique for an Implantable Brain–Machine Interface System

Permalink

https://escholarship.org/uc/item/0zp167g7

Journal

IEEE Journal of Solid-State Circuits, 54(6)

ISSN

0018-9200

Authors

Lee, Mao-Cheng
Karimi-Bidhendi, Alireza
Malekzadeh-Arasteh, Omid
et al.

Publication Date

2019-06-01

DOI

10.1109/jssc.2019.2899521

Copyright Information

This work is made available under the terms of a Creative Commons Attribution License, availalbe at https://creativecommons.org/licenses/by/4.0/

Peer reviewed

eScholarship.org Powered by the California Digital Library
University of California

A CMOS MedRadio Transceiver with Supply-Modulated Power Saving Technique for an Implantable Brain-Machine Interface System

Mao-Cheng Lee, *Student Member, IEEE,* Alireza Karimi-Bidhendi, *Student Member, IEEE,* Omid Malekzadeh-Arasteh, *Student Member, IEEE,* Po T. Wang, *Member, IEEE,* Zoran Nenadic, *Senior Member, IEEE,* An H. Do and Payam Heydari, *Fellow, IEEE*

***Abstract*—A MedRadio 413–419 MHz Inductorless transceiver (TRX) for an implantable brain-machine interface (BMI) in a 180 nm CMOS process is presented. Occupying 5.29 mm^2 of die area (including pad ring), this on-off-keying (OOK) TRX employs a non-coherent direct-detection receiver (RX), which exhibits a measured in-band noise figure (NF) of 4.9 dB and S_{11} of –13.5 dB. An event-driven supply modulation (EDSM) technique is introduced to dramatically lower the RX power consumption. Incorporating an adaptive feedback loop, this RX consumes 42/92 μW power from 1.8 V supply at 1/10 kbps data-rates, achieving –79/–74 dBm sensitivities for 0.1% bit-error-rate (BER). The TX employs a current-starved ring oscillator with an automatic frequency calibration loop, covering 9% supply-voltage variation and 15–78°C temperature range which guarantees operation within the emission mask. The direct-modulation TX achieves 14% efficiency for a random OOK data sequence at –4 dBm output power. Wireless testing over a 350 cm distance accounting for bio-signal data transfer, multi-user coexistence, and *in-vitro* phantom measurement results are demonstrated.**

***Index Terms*—Brain-machine interface (BMI), CMOS, transceiver (TRX), MedRadio band, event-driven supply modulation (EDSM), multi-user coexistence, *in-vitro* phantom.**

I. Introduction

IMPLANTABLE medical devices, such as deep brain stimulators [1] or responsive neurostimulators [2], are routinely used for the treatment of neurological conditions. As technology advances, these systems are also becoming more sophisticated, and this trend will continue in the future. In addition, current brain implants will likely be re-purposed or redesigned in the future to address unmet clinical needs [3]. To fulfill their role, these future implantable systems will need to be endowed with additional features and functions.

One such novel clinical application is the restoration of motor function after stroke or spinal cord injury (SCI) using brain-machine interfaces (BMIs). Generally, BMIs record, process, and decode cortical signals in real time, and use this information to control external devices [4]. This enables those with paralysis to operate prostheses [5] or muscle stimulators [6] directly from the brain while bypassing the neurological injury.

Current state-of-the-art invasive BMIs are mostly used in a laboratory setting, and their clinical adoption will critically depend on the ability to make them fully implantable. Namely, despite encouraging results [7], these systems rely on external electronics and skull-protruding components, which makes them impractical, less safe, and generally unsuitable for everyday at-home use. These obstacles can be circumvented by designing a fully implantable BMI with internal electronics and no skull-protruding components.

Fig. 1 shows an example of a hypothetical implantable BMI system for restoration of walking in individuals with SCI. This system comprises a skull unit for brain signal sensing and a chest-wall unit (CWU) for signal processing. μV-level brain signals sensed by the skull unit are routed out of the head by a subcutaneous tunneling cable (similar to modern deep-brain stimulators [8]), and delivered to the CWU. The CWU processes brain signals to detect walking intentions and converts them into 1–10 kbps wireless commands for external prostheses, such as robotic exoskeletons or functional electrical stimulators. A major design challenge for this system is then to perform signal processing and wireless data transmission tasks, while meeting the size, power, and magnetic resonance imaging (MRI) compatibility constraints necessary for safe human implantation. This includes trading off the power consumption of the DSP and TRX modules. For example, wireless communication between the implantable devices and external computers is typically a power-hungry process. Therefore, minimizing the power consumption of the wireless TRX would enable allocation of a higher fraction of the overall power budget to the brain signal processing units within the CWU. Based on our preliminary estimate, the proposed CWU should consume less than 50 mW for which DSP, data converter and other modules account for 80-90% of total budget and with the remainder allocated to the TRX block. Additionally, limited enclosure area requires small form factor for all wireless unit's constituent components including the antenna. Also, to meet the most stringent field conditions (i.e. static magnetic field stength, specific absorption rate,

Mao-Cheng Lee, Alireza Karimi-Bidhendi, Omid Malekzadeh-Arasteh and Payam Heydari are with the Department of Electrical Engineering and Computer Science, University of California, Irvine, CA 92697, USA (e-mail: maochenl@uci.edu).

Po T. Wang is with the Department of Biomedical Engineering, University of California, Irvine, CA 92697, USA.

Zoran Nenadic is with the Department of Biomedical Engineering and Department Electrical Engineering and Computer Science, University of California, Irvine, CA 92697, USA.

An H. Do is with the Department of Neurology, University of California, Irvine, CA 92697, USA.

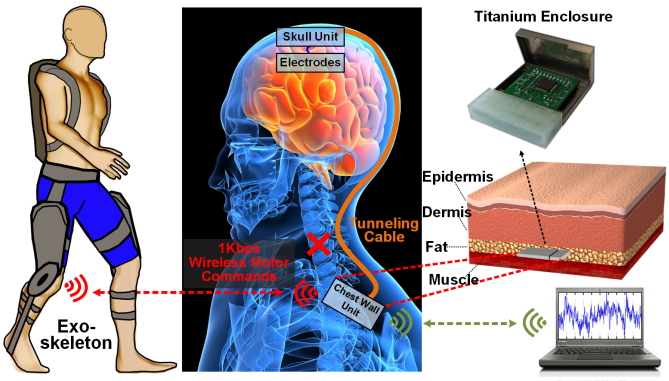

Fig. 1. Proposed fully-implantable BMI system for restoration of walking, with a signal acquisition front-end (skull unit) and signal processing and wireless communication modules (chest wall unit). This system bypasses the injured spinal cord and enables direct brain control of an exoskeleton.

etc.) due to interactions with magnetic field of MRI system, the proposed CWU in Fig. 1 relies on an inductorless TRX with no off-chip component except an antenna. Commercially available MRI-conditional devices use customized structures to enclose antenna to further reduce magnetic interaction and hence satisfy the MRI requirements for implantable systems (e.g., Medtronic W1DR01/W1SR01 [9]).

Multiple telemetry methods – such as near-field magnetic coupling, conduction through the body, and short-range RF communication – exist that establish the link between the implanted device and external units or actuators. Human body communication (HBC defined in IEEE 802.15.6 standard) uses human body as a channel, and has emerged as a promising method for low power and relatively high data rate (>1 Mb/s), while being free from shadowing effect. However, challenges such as interference, difficulty in estimating the channel, impedance variation of skin-electrode interface, and mutipath problem have to be addressed for this method to become widespread [10], [11]. IEEE 802.15.4 bluetooth low energy (BLE), and IEEE 802.15.6 narrowband (NB) and ultra wideband (UWB) PHYs standards have been developed for short-range radios and cover low-power applications (e.g., wireless personal area network and wireless body area network). These standards employ duty cycling for power saving and interference mitigation. While low-power, the radios based on these standards still do not satisfy the severe power budget, heat dissipation, low emission power, and small area constraints required for an implantable BMI system such as the one in Fig. 1.

Several low-power TX/RX architectures were proposed aiming for different applications. ⟵ not sure what this sentence is trying to convey! Are you still talking about implantables? A near-field radio for syringe-implanted sensor nodes was presented in [12] which implemented a communication protocol that eliminated the need for symbol boundary synchronization in the sensor RX. The asymmetric nature of the architecture shifts the performance burden (i.e., high sensitivity RX and high power TX) toward the base station [12]. The N-path uncertain-IF and dual-IF architectures proposed in [13], [14] conduct high-Q selectivity frequency translation without the power-hungry phase-locked loop (PLL). A TX-referenced RX published in [15] improves the interference robustness, and breaks the tradeoff between power, sensitivity, and linearity. A two-tone TRX using a simple envelope-detection RX and a direct-modulation TX was presented in [16].

MedRadio band (401–406 MHz) was dedicated by the Federal Communications Commission for implantable and wearable devices, which has been expanded recently by allocating four 6-MHz bands at 413–419 MHz, 426–432 MHz, 438–444 MHz and 451–457 MHz. Recently published MedRadio TRXs in [17]–[20] employed a bulky on- or off-chip inductor for impedance matching and/or performance improvement. Expanding on our prior work in [21], this paper presents analysis and design of a CMOS low-power inductorless OOK TRX for the MedRadio 413–419 MHz band intended for transferring the BMI control commands and monitoring biosignals wirelessly. A novel event-driven supply modulation (EDSM) technique on the RX side (see Sections III and IV) and a fast start-up power-cycling capability on the TX side (see Section V) are utilized.

Fig. 2. The architecture of the proposed low-power OOK TRX

II. TRX Architecture

Fig. 2 demonstrates the proposed MedRadio TRX comprising a supply-modulated non-coherent direct-detection RX and a direct-modulation OOK TX. On the RX side, the incoming signal is strobed by a periodically-activated noise canceling low-noise amplifier (LNA) above the Nyquist rate of the baseband (BB) signal representing the BMI control commands. The BB signal is then recovered after passing through a class-AB envelope detector and a dynamic latched comparator, as a decision circuitry. A feedback control circuit turns off the RX amplifiers as soon as the current bit is resolved, effectively duty-cycling the RX. As will be illustrated in Section III, this approach will minimize the average power consumption with minor degradation ($\sim$ 5dB per 1 decade increase in data rate) in RX sensitivity. On the TX side, the BB data modulates the free-running digitally controlled oscillator (DCO) incorporating a fast frequency calibration loop, which allows the entire TX to be power-cycled. The OOK modulated signal is amplified by a self-biased, inverter-based power amplifier (PA), and is subsequently delivered to an off-chip antenna (for testing purpose only).

III. Asynchronous Event-Driven Supply Modulation

A conventional direct-detection RX continuously senses, amplifies, and detects the envelope (or power) of the received signal [22], [23]. Following the envelope detection, the clocked comparator generates the BB data. However, the power-hungry blocks, namely, LNA and gain stages – operating at high current levels for noise and power matching purposes – are always activated during the entire detection/comparison phase irrespective of BB signal activities. A number of duty-cycling-based power reduction techniques have been presented [24], [25] to periodically switch off power-hungry blocks with an

Fig. 3. (a) Envelope detector based receiver with a fixed pulse-width. (b) The proposed EDSM receiver with adaptive feedback control loop.

Fig. 4. (a) Event-Driven supply modulated RX schematic. (b) The timing diagram of EDSM RX.

enable signal. The average power consumption of the duty-cycled RX is approximated as:

$$P_{avg} = P_T \times (\frac{2T_{on}}{T_b}) \times OSR + P_{bias} \quad (1)$$

where P_T is the total power consumption of the RX core without duty-cycling technique, T_{on} represents the RX on time, T_b denotes the bit period, and OSR is the oversampling ratio. P_{bias} is power consumption of the bias generation circuit. Clearly, the duty-cycling technique leads to significant amount of power saving if $T_{on} \ll T_b$. However, the supply switching in prior work is done at a fixed pulse-width $T_{on,fix}$ (indicated in Fig. 3(a)) which must account for worst case conditions, i.e., lowest LNA gain, largest comparator metastability time-constant, and signal propagation delay uncertainty across process, voltage, and temperature (PVT) variation. As a result, the amount of power saving is severely limited by this non-optimal $T_{on,fix}$.

To overcome the power-saving limitation due to $T_{on,fix}$ and further reduce T_{on}, we first study the parameters affecting it. T_{on} is approximately lower-bounded by: $T_{on} \geq T_{on,min} (= T_{AMP} + T_{p,ED} + T_{CMP})$. T_{AMP} denotes the time taken for the duty-cycled amplifier to reach its stable dc-bias point at the rising edge of the EN signal shown in Fig. 3(b). $T_{p,ED}$ is the input-output propagation delay of the envelope detector. T_{CMP} represents the time taken by the comparator to make a decision. For the dynamic comparator adopted in this design (see Fig. 4(a)), T_{CMP} is readily derived to be:

$$T_{CMP} \cong \frac{2|V_{THP}|C_L}{I_{SS,1}} - \frac{C_L}{G_m} \ln(\Delta V_{IN}) \quad (2)$$

where V_{THP} indicates the PMOS threshold voltage, $I_{SS,1}$ is the tail current, M_1. C_L is the load capacitor seen at the output of the comparator. G_m represents the equivalent large-signal transconductance of each cross-coupled CMOS inverter (M_4-M_8 and M_5-M_9) realizing regenerative load of the comparator. ΔV_{IN} is the comparator's input amplitude and T_f is a fixed time which is determined by the bias current, the load capacitor, and input device parameters. T_{CMP} is signal dependent, whereas T_{AMP} and $T_{p,ED}$ are both functions of PVT and may vary from chip to chip. T_{AMP} can constitute an increasingly larger portion of T_{on}, eventually limiting the functionality of the EDSM-based RX to data rates below 0.5 Mbps. In this case, techniques such as bias pre-charge should be used in the amplifiers to minimize T_{AMP} and $T_{p,ED}$.

The functional block diagram of the EDSM-based RX is depicted in Fig. 3(b) in which an adaptive feedback control loop (details in Section IV) is employed to guarantee duty-cycling at $T_{on} = T_{on,min}$. Similar to the conventional architecture, upon envelope-detection and the BB data recovery, the feedback control unit will capture the comparison result and generates the control pulses to turn off the power-hungry blocks, thereby lowering the average power consumption. Unlike the duty-cycled RX architectures with constant on time (Fig. 3(a)), the EDSM technique generates control pulses whose pulse-widths vary with $ED_{out} - V_{ref}$ at the comparator inputs. More precisely, the falling edge of these pulses are automatically adjusted depending on the RF signal power, the amplifier gain, and the envelope detection responsivity across PVT variation as soon as the comparator decision has been made (Fig. 3(b)). In summary, this technique optimizes the turn-off edge of EN signal to minimize T_{on}, thereby achieving the lowest power consumption.

IV. Receiver Implementation

The system architecture of the EDSM RX is shown in Fig. 4(a). An event detection circuitry and a delay control unit generate and adjust variable duty-cycle power-switching pulses $SM_{\phi 1}$ for amplifiers and settling-time accelerating pulses $SM_{\phi 2}$ for envelope detector. The system clock (CLK_{SYS}) is provided by an external source (a crystal oscillator (XTAL) in this design). The external source will be provided by a micro-controller, once this TRX is integrated with the CWU. Running at Nyquist rate of the BB signal, CLK_{SYS} periodically turns on the LNA to strobe the received signal. A delayed version of CLK_{SYS}, CLK_{CMP}, triggers the clocked comparator and marks an "event," T_{CMP} seconds after its positive edge (*cf.* Fig. 4(b)). During the event interval, the outputs are captured in an SR latch and are also fed to the event detection circuitry. Enabled by CLK_{SYS}, the event detection circuit generates the falling edges of $SM_{\phi 1}$ once it senses an event, and subsequently turns off the power-hungry LNA and amplifiers until the next strobing edge (set by the positive edge of CLK_{SYS}).

While the linearity requirement of a direct-detection OOK RX is relaxed, its noise performance deserves attention. The noise analysis of a direct detection RX is more involved as the inherent nonlinearity of the ED causes whole host of issues, such as the noise self-mixing phenomenon. Although the commonly used noise-equivalent power (NEP) provides a more accurate evaluation of an ED's noise performance especially at high frequencies, it is not straightforward to relate it to the overall NF of the RX. We thus define the conversion gain (See Section IV-B) to characterize noise and signal frequency-translations in an ED. The RF noise at the ED input will be translated to low frequency at the output through its conversion gain. On the other hand, the low frequency noise within the ED bandwidth is amplified by a large and linear DC gain. The RX chain's NF is derived as follows:

$$NF_{RX} = NF_{amp} + \frac{\overline{V_{n,ED}^2} + \overline{V_{n,LF}^2} A_{ED,DC}^2}{4kTR_s A_V^2 A_{ED}^2} \quad (3)$$

$\overline{V_{n,LF}^2}$ and $\overline{V_{n,ED}^2}$ are the low-frequency noise power at the ED input and the noise contribution of the ED, respectively. NF_{amp} is the NF of amplification chain, A_V is the voltage gain of the entire amplification chain, $A_{ED,DC} = V_{o,DC}/V_{in,DC}$ and $A_{ED} = V_{o,DC}/V_{in,RF}$ are the DC and conversion gains of the ED, respectively.

Fig. 5. The schematic of noise canceling low-noise amplifier, capacitively-degenerated cascaded gain stage unit and differential to single-ended buffer.

Fig. 6. (a) The simulated gain of each stage in the receiver chain. (b) The simulated gain curves of receiver in different gain-modes.

A. Noise Canceling LNA and Gain Stages

Fig. 4 shows the overall RX front-end consisting of a noise-canceling LNA, cascaded gain stage unit(s), differential to single-ended buffers and a gain-mode selector. To cover an adequate TX-RX link range, three distinct parallel paths accommodating low, medium, and high gain-modes are considered in this design. The use of three gain paths instead of VGA allows for noise and power optimization of devices in each path distinctly, resulting in better power efficiency [26]. The gain mode can be selected through a digital automatic gain control in the back-end processor. Fig. 5 shows the LNA schematic, which is based on [27]. The common-gate stage M_1 provides a resistive 50-Ω matching to the antenna. Furthermore, the common-gate and common-source branches have been biased to have identical output common-mode operation. The noise contribution of M_1 is nullified if $g_{m1}R_1 = g_{m2}R_2$. This LNA's NF is readily derived to be:

$$NF_{LNA} = 1 + \frac{R_s}{R_3} + \gamma\frac{R_2}{R_1} + \frac{R_s}{R_1} + \frac{R_sR_2}{R_1^2} \tag{4}$$

where γ is the MOS thermal noise coefficient. The LNA is followed by a capacitively-degenerated differential amplifier and a differential to single-ended buffer. The simulated gain plots of the RX front-end, the LNA, and the amplification stage for the medium-gain mode are shown in Fig. 6(a). Fig. 6(b) depicts the simulated gain plot of the RX front-end under different gain-modes. The RX provides 30 dB (from 40–70 dB) gain adjustment range at 416 MHz.

B. Envelope Detector and Offset Calibration

The active differential-input envelope (power) detectors (e.g., [28] [29]) achieve high responsivity at the expense of common-mode noise accumulation. Fig. 7(a) shows an active differential-input push-push envelope detector. The envelope detector output is the sum of average signal and noise powers (V_{in}^2 and $\overline{V_{CM,noise}^2}$), inducing an unwanted rms voltage drop, A_{noise}, to the output. Fig. 7(b) shows a common-source-based single-ended envelope detector. This detector is preceded by the last-stage differential to single-ended buffer in Fig. 5, which mitigates the common-mode noise accumulation. Fig. 8(a) shows the schematic of the envelope detector used in this design. Assuming the long-channel MOS model and filtering of fundamental and high-order harmonics of the input, the output voltage of this envelope detector is expressed as:

$$V_{o,DC} = ED_{OUT} - V_{REF} = \frac{1}{4}\mu_n C_{ox}\left(\frac{W}{L}\right)_1 R_3 V_{im}^2 \tag{5}$$

where V_{im} denotes the RF input amplitude. At MedRadio frequencies, the power gain is abundance, and thus, the direct-drive interstrage RF connections with no matching network is utilized. This also means ED's conversion gain, A_{ED}, provides more insight about the ED performance rather than its responsivity $\Re$ ($= V_{o,DC}/P_{in,RF}$).

Fig. 7. The output voltage level with input signal with common-mode noise in (a) active differential architecture. (b) differential-to-single first approach.

Fig. 8. (a) The proposed envelope detector schematic. (b) simulated envelope detector output amplitude with different input amplitude. (c) simulated output DC voltage vs. input bias voltage.

$$A_{ED} = \frac{1}{4}g_{m1}R_3\frac{V_{im}}{V_{OD}} = \frac{1}{4}A_{ED,DC}\frac{V_{im}}{V_{OD}} \tag{6}$$

where V_{OD} and g_{m1} are the overdrive voltage and transconductance of transistor M_1 in the circuit of Fig. 8(a). The simulated output vs. input amplitude of this detector is shown in Fig. 8(b), which follows the anticipated square-law transfer characteristic.

Fig. 8(a) shows the envelope detector's input voltage and drain current (approximated by periodic rectified cosine function). Maximizing the second harmonic current will maximize the conversion gain and thus minimize the NEP. Using the analytical study in [30], the second harmonic current in terms of the peak drain current I_{max} and conduction angle $\phi\left(= 2cos^{-1}\left(\frac{V_{TH}-V_{bias}}{V_{im}}\right)\right)$ is obtained:

$$I_2 = I_{\max}\frac{2\sin^3\frac{\phi}{2}}{3\pi(1-\cos\frac{\phi}{2})} \tag{7}$$

I_2 is maximized for $\phi = \pi$, resulting in $V_{bias,opt} = V_{TH}$. This means that the ED should operate as a deep class-AB stage to maximize conversion gain, thus relaxing the sensitivity constraints of the following comparator. Fig. 8(b) presents the simulated envelope detector output amplitude with different input amplitude. Fig. 8(c) shows the simulated output DC voltage vs. input bias voltage of the envelope detector for five different values of the input amplitude. As shown in Fig. 8(c), biasing transistor M_1 around its threshold voltage (≈0.45 V) will maximize the conversion gain.

The ouput thermal noise of envelope detector is derived as follow:

$$\overline{V_{n,ED}^2} = 4kTR_3(1 + \gamma g_{m1}R_3) \tag{8}$$

As mentioned before, the undesired low-frequency noise in the passband of the envelope detector is amplified by $A_{ED,DC}$.

It is worth noting that the single-ended structure in Fig. 8(a) is sensitive to the offset of the following comparator. To overcome this problem, an 8-bit offset-calibration circuit incorporating a successive approximation register (SAR) feedback loop is utilized (see Fig. 9). Based on the comparator output logic level, the SAR control logic determines the output of the 8-bit DAC to compensate for the input-referred offset of the dynamic comparator, capturing up to ±190 mV input-referred comparator offset within 0.3 ms. Fig. 9 compares the statistical input-referred offset voltages of the comparator with and without this calibration scheme using Monte-Carlo simulation. From the Monte-Carlo simulation with 300 different samples, the result shows a 38-fold improvement (i.e., σ is reduced from 86.6 mV to 2.3 mV).

Fig. 9. Offset calibration system and Monte-Carlo simulation results.

Fig. 10. The settling time of (a) conventional envelope detector. (b) the proposed envelope detector with acceleration switch.
Fig. 11. (a) The schematic of proposed direct-modulation transmitter. (b) Measured TX output power spectrum. (c) AFC block diagram.

C. Settling-Time Acceleration Switch

The amount of power saving in this RX is directly dependent on its ability to function properly within extremely short T_{on}'s. However, since the EDSM scheme turns amplifier stages on and off in every clock cycle, the voltage level at the output of the envelope detector slews up too slowly to reach its default value, causing the comparison error at the comparator. Depicted in Fig. 10(a), the charging of the decoupling capacitor C_1 during the off-to-on dc-bias transition at the output of the buffer would induce a glitch at the gate of M_1, causing a large transient voltage drop at the output. Fig. 10(b) shows the envelope detector incorporating two settling-time acceleration switches SW_1 and SW_2 to shorten the settling-time. To hold the charge across C_1 constant, the delay control unit applies a delayed version of $SM_{\phi 1}$ to SW_1 and SW_2. This avoids the voltage change at the gate/drain of M_1 during the control-signal transition and thus considerably reduces the envelope detector settling time.

V. Transmitter Implementation

A. Direct-Modulation Transmitter

The MedRadio band at 413–419 MHz relaxes carrier frequency stability requirement, particularly for constant-amplitude modulation schemes. Shown in Fig. 11(a), the proposed TX chain is comprised of a free-running DCO with automatic frequency calibration (AFC), OOK-modulating T-switch, and power-configurable inverter-based driver and PA circuits. Fast startup time of the DCO allows for the whole TX to be power-cycled which not only saves power, but also avoids unnecessary power emission when transmitting 0s. The entire PA circuit following the DCO consists of a self-biased inverter followed by a tapered chain of 8-parallel inverter-based drivers and the PA, all biased at half-V_{DD}. The TX output power can be configured from -4 to 4.5 dBm using 8-bit driver and PA switches. Fig. 11(b) shows the measured TX power spectrum in the continuous-wave (CW) operation. With the design parameter values listed in Fig. 11(a), the T/R switch shows –1.2 dB insertion loss at –4 dBm output power.

B. Current Starved Ring Oscillator with AFC Loop

To achieve low power operation, a 5-stage current starved ring oscillator with digital AFC [31] is designed (Fig. 11(c)). The oscillation frequency, f_{osc}, is controlled by 5-bit coarse- and 5-bit fine-tuned current mirrors from SPI and the AFC loop, respectively, to compensate for PVT variations. Within AFC block, the 13-bit counter computes the binary representation of divide-by-two oscillation frequency by counting its cycles over the 32.768 kHz reference clock period provided by a Pierce crystal oscillator (shared by the RX). The result is compared with the target cycle count N_{CYC}, where $N_{CYC} = f_{osc}/(2f_{XTAL})$, and fed to a SAR logic to adjust the oscillator current. The tuning range is $\Delta f = 2^B LSB$, where LSB is the fine tuning resolution (2.5 MHz in this work) and B is the number of control-bits in SAR algorithm (5 in this work). Besides, the calibration algorithm allocates one clock period for counting window, one for comparison and one for internal reset. Therefore, the total calibration time T_{cal} is derived as: $T_{cal} = 3 \times B/f_{XTAL}$. For our application, this AFC-backed DCO was implemented to achieve fine-tuning across 80 MHz frequency range within an estimated 0.47 ms calibration time.

VI. Experimental Results

Designed and fabricated in a 180 nm CMOS technology, this TRX occupies 2.35 $\times$ 2.25 mm^2 of die area including pads (Fig. 12). The functionality of the TRX was verified by both electrical and *in-vitro* phantom measurements. The system-level measurement include wireless testing for TX-RX distances varying from 25–350 cm as well as wireless transferring of pre-recorded bio-signals. Additionally, the coexistence testing in multi-user setting was conducted.

A. Receiver Electrical Measurements

Fig. 13(a) presents the measured BER at 1- and 10-kbps data-rates using PN15 data sequence at 1.5-V supply voltage. The BER stays below 0.1% for the input power larger than –79 and –74 dBm at 1- and 10-kbps data-rates in the high-gain mode, respectively. Link-budget calculation reveals that to maintain the wireless operation at BER's below 0.1% over short distances down to 25 cm, the RX should tolerate a maximum input power larger than –28.8 dBm. Fig. 13(b) shows measured transfer characteristic and BER vs. input power under the RX's low-gain mode. The measured P_{1dB} is –28.5 dBm. Moreover, BER stays below 0.1% for input powers from –62 to –25 dBm, resulting in an overall dynamic range from –79 to –25 dBm across all gain modes. Fig. 13(c) shows both simulated and measured NF and S_{11} vs. frequency. The EDSM RX achieves –13.5 dB S_{11} and 4.9 dB NF at 416 MHz, respectively, without any on/off chip inductor.

Table I shows the measured power consumption of each RX block before and after applying EDSM technique. The EDSM technique is capable of reducing the RX power by 99.6% to 42 μW at 1 kbps and by 99.1% to 92 μW at 10 kbps.

B. Transmitter Electrical Measurements

Fig. 13(d) shows both measured and simulated overall TX efficiency vs. output power for OOK modulated signal. The TX output power varies from –4 to 4.5 dBm with efficiency varying from 14% to 36%. In the CW mode, the efficiency varies from 7% to 18%, since for half the time the data

Fig. 12. Chip micrograph with main circuit blocks labeled.

TABLE I
Measured Transceiver Power Consumption Breakdown

Block	Before EDSM	After EDSM
LNA	5.8 mW	17.3 μW
AMPs	3.8 mW	9.2 μW
BUF+ED	0.6 mW	9.8 μW
CMP	4.2 μW	4.2 μW
Total	10.2 mW	42 μW

Block	OOK Mode
PA	1.69 mW
Driver	0.7 mW
VCO	0.42 mW

Fig. 13. TRX electrical measurement results: (a) Measured BER with different data-rate. (b) Linearity and BER measurement in low-gain mode. (c) Measured S11 and NF. (d) TX efficiency vs. output power.

Fig. 14. Frequency variation before and after using AFC

is 0 and the TX is powered off. TX power breadkdown in the OOK transmission mode is shown in Table I. The AFC periodically monitors the TX carrier frequency. The frequency-drift tolerance is significantly improved from 19% down to 0.24% across 1.73–1.9 V supply interval and from 4.6% down to 0.3% across 15–78°C temperature range (*cf.* Fig. 14).

C. Wireless Connection Measurement Setup and Results

To test wireless connectivity in this work, a 416-MHz PCB loop-antenna was designed and fabricated (Fig. 15(a)). Figs. 15(b)-(c) demonstrate the simulated radiation pattern at 416 MHz and the measured antenna gain and S_{11} vs. frequency, respectively. As is clear from Fig. 15(c), RF band selectivity is partially provided by the antenna. With an emission power of –16 dBm from TX, an antenna gain of –12 dBi, and considering a 35-dB path loss across a 3 m distance at 416 MHz, the RX sensitivity is smaller than –63 dBm. Fig. 16(a) shows the setup for wireless testing. With TX-RX distances of 25–350 cm and for 1–10 kbps data rates, the measured BER always remains <0.1% (Fig. 16(b)). The other wireless testing of the TRX is established by transferring pre-recorded electrocorticogram (ECoG) and electromyogram (EMG) signals at 1-m distance. The transmitted and received time-domain plots of ECoG and EMG signals with BER below 0.01% and 5×10^{-6}% are shown in Figs. 16(c) and (d), respectively.

D. Multi-User Coexistence and Interference Testing

Coexistence of multiple users is an important issue. It is undeniable that the path loss and wireless signal energy absorption of the human tissue will increase with frequency. For example, the human tissue (composed of 2cm skin and fat) will cause around 63 dB attenuation for a 2.4 GHz signal [32]. However, a practical issue of BMI is the potential interference between multiple users operating in the vicinity of one another at the frequency around MedRadio band. Fig. 17 presents the measured interference power over a wide frequency range that causes a BER higher than 0.1%. Compared to other architectures with high-Q internal/external passive components, this inductorless design exhibits a lower interference tolerance. To address this issue, we notice that MedRadio has limited the transmission time of TXs to 0.1% during a specific period. This notion was utilized to implement a listen-before-talk (LBT) protocol with the TRX operating in the burst-mode data transfer (*cf.* Fig. 18(a)). This protocol advances through 10 time-slots in search of an available slot in the presence of an interferer, TRX3, for exclusive pairing of TRX1 and TRX2. An exemplary coexistence scenario is demonstrated in

Fig. 15. (a) PCB including an on-board loop-antenna and TQFP packaged IC. (b) Simulated antenna radiation pattern. (c) Measured antenna gain and S_{11} vs. frequency.

Fig. 16. (a) The setup for wireless connection measurement. (b) The measured BER with different TX-to-RX distance. The transmitted and received (c) ECoG signal. (d) EMG signal.

Fig. 18(b), where the TRX3-TRX2 distance is shorter than the TRX1-TRX2 distance by 0.5 m. This protocol improves BER from 4.53% (continuous mode) down to 0.03% (LBT). Although not implemented here, a frequency-domain LBT protocol can also be adopted as envisioned in the MedRadio standard. This is possible due to wideband operation and large tuning range of this TRX. For the BMI application targeted in this design, wireless communication is primarily intended for transferring a limited number of commands, thus the BER degradation due to the interferers can be further reduced in the backend processor by introducing redundancy in the command data package.

E. in-vitro Phantom Measurements

Figs. 19(a) and (b) present the *in-vitro* wireless connection setup and cross-section of the phantom material, respectively. The dimensions of titanium enclosure and plastic cap is shown in Fig. 19(c). A phantom composed of 3 layers, emulating the conductivity, permittivity and thickness of the human skin, fat, and muscle in chest area [33], [34] is used to emulate the signal attenuation through human tissue. The measured conductivity of skin, fat and muscle layers are 0.77, 0.034, 0.8 S/m, respectively. The measured permittivity of each corresponding layer is 49.1, 5.54 and 57.4, as indicated in Figs. 19(f) and (g). Wireless connectivity was evaluated by positioning TX and RX at various horizontal and vertical distances. The BER remains <0.1% for a maximum vertical distance of 1.8 m. Similarly, the BER remains <0.1% for a maximum horizontal distance of 0.8 m while the position of TRX2 is fixed (as shown in Fig. 19(d) and (e)). Table II and Table III summarize the performance of proposed TRX and comparison with prior art. The non-coherent EDSM RX achieves –79/–74 dBm sensitivity and dissipates 42/92 μW at 1/10 kbps, respectively.

VII. Conclusion

A low-power MedRadio TRX in 180 nm CMOS was presented. An event-driven supply modulation (EDSM) technique was introduced to dramatically lower the RX power consumption. The TRX achieved wireless data transfer up to a distance of 350 cm with BER < 0.1% and low overall power consumption. The multi-user coexistence testing and *in-vitro* phantom measurements also revealed that the TRX can serve as a basis of highly integrated and robust wireless chip, providing a solution for low-power TRX design for an implantable BMI system.

Acknowledgment

The authors thank TowerJazz Semiconductor for chip fabrication, and Dave Huh from Keysight Technologies for providing measurement equipment. This research is funded by the National Science Foundation Awards #1446908 and #1646275.

Fig. 17. The measured interference power causing BER higher than 0.1%

TABLE II
RECEIVER PERFORMANCE COMPARISON

Reference	ISSCC 2011 [35]	JSSC 2012 [16]	ISSCC 2014 [17]	TMTT 2014 [18]	TCAS-I 2016 [19]	JSSC 2016 [13]	JSSC 2016 [15]	This Work
Process (nm)	130	90	40	180	180	65	65	180
Carrier Freq. (MHz)	403	915	402∼405 / 420∼450	403/433	402∼405	2400	915	413∼419
Supply Voltage (V)	1	1	1	1.2	0.45	0.5	1	1.5
Architecture	Low-IF	2-Tones	Zero-IF	Direct Conv.	Low-IF	Dual-IF	TX-referenced	EDSM
Modulation	FSK	OOK	GMSK/DBPSK	ASK	OOK/FSK	OOK	BPSK	OOK
Inductor Type	Off-Chip	On-Chip	Off-Chip	Off-Chip	On-Chip	Off-Chip	Off-Chip	None
Data Rate (kbps)	200	10	11.7/562/4500	10	50/120	10	10	1/10
Sensitivity (dBm)	–70/–90	–56/–83	–112/–93/–83	–72/–73	–55/–53.5	–97	–76	–79/–74
Power	44/120 μW	63[a]/120[a] μW	2.19 mW	2.19 mW	352 μW	99 μW	135 μW	42/92 μW

[a]Excluding FPGA and IF clock generation.

Fig. 18. (a) The flowchart of listen-before-talk protocol adopted in this work and (b) coexistence test setup.

TABLE III
TRANSMITTER PERFORMANCE COMPARISON

Reference	ISSCC 2014 [17]	TMTT 2014 [18]	JSSC 2009 [20]	This Work
Process (nm)	40	180	180	180
Carrier Freq. (MHz)	402∼405 420∼450	403	403	413∼419
Supply (V)	1	1.2	1.8	1.8
Architecture	Polar/Direct Mod.	Direct Mod.	Direct Mod.	Direct Mod.
Modulation	GMSK / DBPSK	OOK / OQPSK	FSK	OOK
Inductor Type	Off-Chip	Off-Chip	On-Chip	None
Output Power (dBm)	–10/–17	–20.9/–17	–20∼0	–4∼4.5
Data Rate (kbps)	11/4500	100/1000	50	1/10
Efficiency	NA	NA	33%[a] @-5 dBm	14%(OOK) 7%(CW)
Power (mW)	2.27/2.28	3.32	4.9	2.8[b] 5.6[c]

[a]PA only. [b]With -4 dBm output power in OOK mode. [c]With -4 dBm output power in CW mode.

REFERENCES

[1] D.-B. S. for Parkinson's Disease Study Group, "Deep-brain stimulation of the subthalamic nucleus or the pars interna of the globus pallidus in parkinson's disease," New England Journal of Medicine, vol. 345, no. 13, pp. 956–963, 2001.

[2] C. N. Heck and D. e. a. King-Stephens, "Two-year seizure reduction in adults with medically intractable partial onset epilepsy treated with responsive neurostimulation: Final results of the RNS system pivotal trial," Epilepsia, vol. 55, no. 3, pp. 432–441, 2014.

[3] M. J. Vansteensel, E. G. Pels, M. G. Bleichner, M. P. Branco, T. Denison, Z. V. Freudenburg, P. Gosselaar, S. Leinders, T. H. Ottens, M. A. Van Den Boom et al., "Fully implanted brain–computer interface in a locked-in patient with als," New England Journal of Medicine, vol. 375, no. 21, pp. 2060–2066, 2016.

[4] J. R. Wolpaw, N. Birbaumer, D. J. McFarland, G. Pfurtscheller, and T. M. Vaughan, "Brain–computer interfaces for communication and control," Clinical neurophysiology, vol. 113, no. 6, pp. 767–791, 2002.

[5] A. H. Do, P. T. Wang, C. E. King, A. Schombs, S. C. Cramer, and Z. Nenadic, "Brain-computer interface controlled functional electrical stimulation device for foot drop due to stroke," in Engineering in Medicine and Biology Society (EMBC), 2012 Annual International Conference of the IEEE. IEEE, 2012, pp. 6414–6417.

[6] C. E. King, P. T. Wang, C. M. McCrimmon, C. C. Chou, A. H. Do, and Z. Nenadic, "The feasibility of a brain-computer interface functional electrical stimulation system for the restoration of overground walking after paraplegia," Journal of neuroengineering and rehabilitation, vol. 12, no. 1, p. 80, 2015.

[7] J. L. Collinger, B. Wodlinger, J. E. Downey, W. Wang, E. C. Tyler-Kabara, D. J. Weber, A. J. McMorland, M. Velliste, M. L. Boninger, and A. B. Schwartz, "High-performance neuroprosthetic control by an individual with tetraplegia," The Lancet, vol. 381, no. 9866, pp. 557–564, 2013.

[8] DBS^{TM}Extension Kit for Deep Brain Stimulation, Medtronic.

[9] "Medtronic Azure MRI SureScan Specifications Sheets." [Online]. Available: https://www.medtronic.com/us-en/healthcare-professionals/products/cardiac-rhythm/pacemakers/azure.html

[10] W. Saadeh, M. A. B. Altaf, H. Alsuradi, and J. Yoo, "A 1.1-mW ground effect-resilient body-coupled communication transceiver with pseudo OFDM for head and body area network," IEEE J. Solid-State Circuits, vol. 52, no. 10, pp. 2690–2702, Oct 2017.

[11] ——, "A pseudo OFDM with miniaturized FSK demodulation body-coupled communication transceiver for binaural hearing aids in 65 nm CMOS," IEEE J. Solid-State Circuits, vol. 52, no. 3, pp. 757–768, Mar. 2017.

[12] Y. Shi, M. Choi, Z. Li, Z. Luo, G. Kim, Z. Foo, H. Kim, D. D. Wentzloff, and D. Blaauw, "A 10 mm^3inductive coupling radio for syringe-implantable smart sensor nodes," IEEE J. Solid-State Circuits, vol. 51, no. 11, pp. 2570–2583, Nov 2016.

[13] C. Salazar, A. Cathelin, A. Kaiser, and J. Rabaey, "A 2.4 GHz interferer-resilient wake-up receiver using a dual-IF multi-stage N-path architecture," IEEE J. Solid-State Circuits, vol. 51, no. 9, pp. 2091–2105, 2016.

[14] N. M. Pletcher, S. Gambini, and J. Rabaey, "A 52 μW wake-up receiver with $-$ 72 dbm sensitivity using an uncertain-IF architecture," IEEE J. Solid-State Circuits, vol. 44, no. 1, pp. 269–280, Jan 2009.

[15] D. Ye, R. van der Zee, and B. Nauta, "A 915 MHz 175 μW receiver using transmitted-reference and shifted limiters for 50 dB in-band interference tolerance," IEEE J. Solid-State Circuits, vol. 51, no. 12, pp. 3114–3124, 2016.

[16] X. Huang, A. Ba, P. Harpe, G. Dolmans, H. de Groot, and J. R. Long, "A 915 MHz, ultra-low power 2-tone transceiver with enhanced interference resilience," IEEE J. Solid-State Circuits, vol. 47, no. 12, pp. 3197–3207, Dec 2012.

[17] M. Vidojkovic, X. Huang, X. Wang, C. Zhou, A. Ba, M. Lont, Y. H. Liu, P. Harpe, M. Ding, B. Busze, N. Kiyani, K. Kanda, S. Masui, K. Philips, and H. de Groot, "A 0.33nJ/b IEEE802.15.6/proprietary-MICS/ISM-band transceiver with scalable data-rate from 11kb/s to 4.5Mb/s for medical applications," in IEEE Int. Solid-State Circuits Conf. Dig. of Tech. Papers (ISSCC), 2014, pp. 170–171.

[18] H. C. Chen, M. Y. Yen, Q. X. Wu, K. J. Chang, and L. M. Wang, "Batteryless transceiver prototype for medical implant in 0.18-μm CMOS technology," IEEE Trans. Microwave Theory Tech., vol. 62, no. 1, pp. 137–147, Jan 2014.

[19] J. Y. Hsieh, Y. C. Huang, P. H. Kuo, T. Wang, and S. S. Lu, "A 0.45-v low-power OOK/FSK RF receiver in 0.18 μm CMOS technology for implantable medical applications," IEEE Trans. Circuits Syst. I Reg. Papers, vol. 63, no. 8, pp. 1123–1130, 2016.

[20] N. Cho, J. Bae, and H. J. Yoo, "A 10.8 mW body channel communication/mics dual-band transceiver for a unified body sensor network controller," IEEE J. Solid-State Circuits, vol. 44, no. 12, pp. 3459–3468, 2009.

[21] M. C. Lee, A. Karimi-Bidhendi, O. Malekzadeh-Arasteh, P. T. Wang, Z. Nenadic, A. H. Do, and P. Heydari, "A CMOS inductorless MedRadio OOK transceiver with a 42 μW event-driven supply-modulated RX and a 14% efficiency TX for medical implants," in IEEE Custom Integrated Circuits Conf. (CICC), April 2018, pp. 1–4.

[22] L. C. Liu, M. H. Ho, and C. Y. Wu, "A medradio-band low-energy-per-bit CMOS OOK transceiver for implantable medical devices," in IEEE Biomed. Circuits Syst. Conf. (BioCAS), Nov 2011, pp. 153–156.

Fig. 19. (a) *in-vitro* phantom measurement setup. (b) The cross-section of the phantom material. (c) The dimension of titanium box and plastic cap. (d) The measured BER results with different vertical distance. (e) The measured BER results with different horizontal distance. (f) Phantom layers conductivity vs. frequency. (g) Phantom layers dielectric constant vs. frequency.

[23] C. W. Chou, L. C. Liu, and C. Y. Wu, "A MedRadio-band low-energy-per-bit 4-Mbps CMOS OOK receiver for implantable medical devices," in 35th Annu. Int. Conf. IEEE Eng. Med. Biol. Soc. (EMBC), July 2013, pp. 5171–5174.

[24] H. Milosiu, F. Oehler, M. Eppel, D. Frühsorger, S. Lensing, G. Popken, and T. Thönes, "A 3-μW 868-MHz wake-up receiver with -83 dBm sensitivity and scalable data rate," in Proc. 39th Eur. Solid-State Circuits Conf. (ESSCIRC), Sept 2013, pp. 387–390.

[25] D. Y. Yoon, C. J. Jeong, J. Cartwright, H. Y. Kang, S. K. Han, N. S. Kim, D. S. Ha, and S. G. Lee, "A new approach to low-power and low-latency wake-up receiver system for wireless sensor nodes," IEEE J. Solid-State Circuits, vol. 47, no. 10, pp. 2405–2419, Oct 2012.

[26] D. C. Daly and A. P. Chandrakasan, "An energy-efficient OOK transceiver for wireless sensor networks," IEEE J. Solid-State Circuits, vol. 42, no. 5, pp. 1003–1011, May 2007.

[27] F. Bruccoleri, E. A. M. Klumperink, and B. Nauta, "Wide-band CMOS low-noise amplifier exploiting thermal noise canceling," IEEE J. Solid-State Circuits, vol. 39, no. 2, pp. 275–282, 2004.

[28] J. Lee, Y. Chen, and Y. Huang, "A low-power low-cost fully-integrated 60-GHz transceiver system with OOK modulation and on-board antenna assembly," IEEE J. Solid-State Circuits, vol. 45, no. 2, pp. 264–275, Feb 2010.

[29] Z. Wang, P. Y. Chiang, P. Nazari, C. C. Wang, Z. Chen, and P. Heydari, "A CMOS 210-GHz fundamental transceiver with OOK modulation," IEEE J. Solid-State Circuits, vol. 49, no. 3, pp. 564–580, March 2014.

[30] L. Zhou, C. C. Wang, Z. Chen, and P. Heydari, "A W-band CMOS receiver chipset for millimeter-wave radiometer systems," IEEE J. Solid-State Circuits, vol. 46, no. 2, pp. 378–391, Feb 2011.

[31] M. Marutani, H. Anbutsu, M. Kondo, N. Shirai, H. Yamazaki, and Y. Watanabe, "An 18mW 90 to 770MHz synthesizer with agile auto-tuning for digital TV-tuners," in IEEE Int. Solid-State Circuits Conf. Dig. Tech. Papers, Feb 2006, pp. 681–690.

[32] D. Kurup, G. Vermeeren, E. Tanghe, W. Joseph, and L. Martens, "In-to-out body antenna-independent path loss model for multilayered tissues and heterogeneous medium," Sensors (Basel), vol. 15, no. 1, pp. 408–421, dec 2014.

[33] T. Karacolak, A. Z. Hood, and E. Topsakal, "Design of a dual-band implantable antenna and development of skin mimicking gels for continuous glucose monitoring," IEEE Trans. Microwave Theory Tech., vol. 56, no. 4, pp. 1001–1008, 2008.

[34] A. T. Mobashsher and A. M. Abbosh, "Artificial human phantoms: Human proxy in testing microwave apparatuses that have electromagnetic interaction with the human body," IEEE Microwave Mag., vol. 16, no. 6, pp. 42–62, 2015.

[35] J. Pandey, J. Shi, and B. Otis, "A 120μW MICS/ISM-band FSK receiver with a 44μW low-power mode based on injection-locking and 9x frequency multiplication," in IEEE Int. Solid-State Circuits Conf. (ISSCC) Dig. Tech. Papers, Feb 2011, pp. 460–462.